Materials & Design 222 (2022) 111024

Contents lists available at ScienceDirect

Materials & Design

journal homepage: www.elsevier.com/locate/matdes

Bilayered soft/hard magnetic nanowires as in-line writing heads

Vivian M. Andrade [a,b,*], Sofia Caspani [b], Alejandro Rivelles [c], Sergey A. Bunyaev [b], Vladimir O. Golub [d], João P. Araujo [b], Gleb N. Kakazei [b], Célia T. Sousa [b,e], Mariana P. Proenca [c,b,*]

[a] Department of Engineering Physics, Faculty, of Engineering of University of Porto, R. Roberto Frias, s/n, 4200-465 Porto, Portugal
[b] IFIMUP - Institute of Physics for Advanced Materials, Nanotechnology and Photonics, Department of Physics and Astronomy, Faculty of Sciences, University of Porto, Rua do Campo Alegre 678, 4169-007 Porto, Portugal
[c] ISOM and Dpto. Electrónica Física, Universidad Politécnica de Madrid, Avda. Complutense 30, E-28040 Madrid, Spain
[d] Institute of Magnetism NAS of Ukraine and MES of Ukraine, Kyiv 03142, Ukraine
[e] Dpto. de Física Aplicada, Universidade Autónoma de Madrid, 28049 Madrid, Spain

HIGHLIGHTS

- Magnetic coupling between soft/hard layers reduced the reversal field of hard ones.
- FORC diagrams provided a fingerprint to detect magnetically coupled layers.
- In-line writing heads made of coupled bilayers are propitious for future devices.

GRAPHICAL ABSTRACT

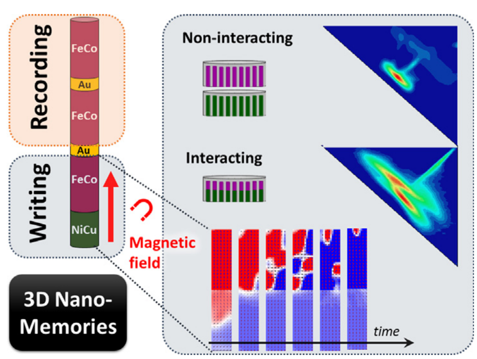

ARTICLE INFO

Article history:
Received 28 February 2022
Revised 25 July 2022
Accepted 1 August 2022
Available online 4 August 2022

Keywords:
Magnetic nanowires
Multisegmented nanostructure
Racetrack memory device
Magnetization reversal modes

ABSTRACT

Multi-segmented cylindrical nanowires (NWs) are the most promising systems for 3D racetrack memory devices, where information is stored as in-line magnetic domains. However, reading and writing information is still a challenge, as external reading/writing heads have to be implemented near the tracks. The writing component should be made of a bilayered soft/hard coupled magnetic system, so that information could be easily written by external magnetic fields. Here, we demonstrate the feasibility of using a $Ni_{90}Cu_{10}/Fe_{20}Co_{80}$ segmented NW as the writing element, in which magnetic information is written by applying external magnetic fields. Using low-cost template-assisted electrodeposition methods, single, bi- and multi-segmented NW hexagonal arrays of NiCu and FeCo/Au were fabricated. A throughout magnetic characterization using magnetic hysteresis loops, ferromagnetic resonance and first-order reversal curves (FORCs) revealed that the soft segment (NiCu) induced the reversal of the hard segment (FeCo) in a two-step process, reducing its coercive and effective anisotropy fields when coupled. Finally, micromagnetic simulations certified the experimental observations of a multi-step reversal process. This work demonstrates the important role of interface interactions for the future implementation of an in-line writing component in a 3D racetrack memory device, enhancing their potential applicability.

* Corresponding authors.
E-mail addresses: vandrade@ifi.unicamp.br (V.M. Andrade), mpproenca@fc.up.pt (M.P. Proenca).

https://doi.org/10.1016/j.matdes.2022.111024
0264-1275/© 2022 Published by Elsevier Ltd.

1. Introduction

The tremendous growth of information needed to be stored in devices that are becoming smaller, constitutes a challenge for the scientific community. Conveniently, the latest advances in nanoscale fabrication and characterization techniques have promoted a boost in the study of metallic, semiconducting and isolating nanomaterials [1–5]. A novel type of storage device, called racetrack memory (RM), has already been proposed as a viable candidate to store non-volatile memory. This device uses magnetic domains to stack the information along magnetic nanostructured stripes, acting, therefore, as bits [6]. The device mechanism relies on the supervised displacement of the pinned magnetic domain walls (DWs) by the application of spin-polarized current pulses, allowing the bit propagation along the track [6–8]. The main advantage of a racetrack device is its potential to achieve performances as high as a conventional solid-state memory device, but at the same low price of a flash drive [9]. However, some limitations still have to be defeated, such as the Walker breakdown and the local Joule heating [10]. It has been shown that the Walker breakdown disappears in cylindrical wires and the use of chemical constraints avoids Joule overheating [11]. Among the prospective candidates, multi-segmented cylindrical magnetic nanowire (NW) arrays using materials with different magnetic properties are interesting not only for RM but also for spintronic and biomedical applications [12–14,4]. Besides their low-cost and simple methods of fabrication, arrays of NWs have successfully demonstrated to be able to overcome the previously mentioned limitations concerning their implementation in RM devices [15–17].

Several authors have already studied multi-segmented cylindrical NWs composed of different materials, such as CoNi/Co [18], Co/Cu [19], FeCo/Cu [20–22], Fe/Cu [23,24], FeCoCu/Cu [25,26], Ni/Co [27,28,25,29] and Ni/Cu [30,31]. Concerning practical applications, the accurate understanding of the role of each layer with distinct structural and magnetic properties is an important path to avoid further issues, such as system overheating or Walker breakdown in RM devices, as previously mentioned. In addition, multi-segmented NWs offer the possibility to integrate a writing element along the storage track (hard segments), made of a bilayered soft/hard coupled magnetic system. Micromagnetic simulations have already demonstrated that this approach promotes a faster way of writing information in 3D RM devices [15]. The magnetic state of the integrated writing heads can be tuned all at once by applying low external magnetic fields. The respective written information can then be selectively recorded into the 3D RM by applying spin-polarized currents through pre-selected tracks. Although these evaluations seem promising, thorough experimental research of multi-segmented NWs with low and high anisotropy components still needs to be performed. This work presents a detailed analysis of the magnetic coupling interactions in soft/hard multi-segmented NWs, aiming their application as integrated writting heads in future 3D RM devices.

The magnetic requirements of the recording components in such devices are high uniaxial magnetic anisotropy and high saturation magnetization [32]. Cylindrical magnetic NWs with small diameters ($<$ 100 nm) and aspect ratios (length/diameter) higher than 1.5 are known to exhibit high uniaxial magnetic anisotropy along the wire axis [33]. FeCo is the binary alloy presenting the highest saturation magnetization and, consequently, higher associated shape anisotropy field [34–37]. Therefore, FeCo with 20% of Fe and 80% of Co will be used as the hard magnetic material (for the recording segments)[38]; while NiCu with 90% of Ni and 10% of Cu will be used as the soft magnet (to be implemented in the writing heads along the racetrack), due to its low parallel coercivity [39]. The choice of these compositions were based on their optimized electrodeposition process, since it was already shown that the stoichiometry can be held almost constant along the template length [38,40]. Previous works on Co/Ni bilayered NWs already demonstrated that the interface interactions lead to a two-step magnetization reversal, where the soft phase induces the switching of the hard element.[28] This coupling between the segments is translated into a fingerprint on the first-order reversal curve (FORC) diagrams, where two clear coercive fields, one for each segment, can be detected although not observed in major magnetic hysteresis loops.[27] In this work, we have introduced two materials with a higher (FeCo) and lower (NiCu) saturation magnetization than Co and Ni, respectively, aiming to increase the soft/hard interface interaction and thus promote a more efficient writing process.

In summary, this work aims to experimentally demonstrate the possibility of using a segmented coupled system as a writing head in a 3D RM device. The proposed system has several advantages. By keeping the diameter constant along the wire's length, it avoids pinning of magnetic DWs at the interface or local increase in current density (when decreasing the diameter), which might lead to unwanted local Joule heating effects. The selected compositions correspond to the softest ($Ni_{90}Cu_{10}$) and hardest ($Fe_{20}Co_{80}$) materials found in cylindrical wires with similar diameters [39,38], broadening the range of writing fields one can use. The incorporation of an in-line writing head will trigger the DW nucleation at one extremity of the wire as opposed to the stochastic magnetic reversal behaviour reported in multisegmented magnetic/non-magnetic NWs [41].

A detailed evaluation of the magnetic reversal mechanisms is here presented for single, bi- and multi-segmented $Ni_{90}Cu_{10}$ and $Fe_{20}Co_{80}$ NWs. First, single and bi-segmented NWs are studied by major magnetic hysteresis loops, ferromagnetic resonance and FORC analysis, where evidence of soft/hard magnetic coupling was found. The throughout magnetic characterization together with micromagnetic simulations revealed that the soft segment promotes the magnetic reversal of the hard segment for the coupled bi-segmented layer. By introducing thin Au layers as chemical constraints between the FeCo hard segments, in a multi-segmented NiCu/[FeCo/Au(20 nm)]$_3$ system, the activation of the reversal is still detected. A significant reduction of the parallel coercive field is observed and a two-branch FORC fingerprint is still present. These results demonstrate the strong interaction effect between NiCu and FeCo segments, revealing that the use of such a system can overcome some of the existent issues for practical applications of RM.

2. Experimental details

2.1. Sample preparation

Nanoporous alumina templates were obtained by a two-step anodization process of electropolished high-purity aluminum foils (99.999%, Goodfellow GmbH, Hamburg, Germany) following previous reports [42,1]. First and second anodizations were performed in 0.3 M oxalic acid at 40 V and 4°C for 24 and 60 h, respectively. Prior to the electrodeposition process, the Al was chemically etched in 0.2 M $CuCl_2$ + 0.1 M HCl aqueous solution at room temperature, and the alumina barrier layer at the pores' bottom removed by floating the template in 0.5 M H_3PO_4 at 40°C for ~40 min. Reagents and solvents were purchased from Sigma–Aldrich (Merck KGaA, Darmstadt, Germany) with a purity range of 97–99%.

The NW arrays were grown by DC electrodeposition inside the alumina templates using a three-electrode setup with a Pt electrode as the counter electrode, Ag/AgCl (in 4 M KCl) as the reference electrode, and an Au sputtered layer as the working electrode. Different electrolytes were used for each material deposited: *1)* Orosene E 4 g/L (from Italgalvano SPA, Lodi Vecchio, Italy) for the Au segments; *2)* 0.16 M $CoSO_4$ + 0.04 M $FeSO_4$ + 0.16 M HBO_3 + 0.06 M $C_6H_8O_6$ for FeCo [38]; and, *3)* 0.35 M $NiSO_4$ + 0.02 M $CuSO_4$ + 0.3 M HBO_3 for NiCu [39]. All electrodepositions were performed at room temperature by applying a constant potential of −1.0 V for NiCu and Au and −1.8 V for FeCo layers using a Sourcemeter (Keithley 2400C). A deposition rate of ~200 nm/min and ~700 nm/min were obtained for $Ni_{90}Cu_{10}$ and $Fe_{20}Co_{80}$ alloys, respectively, as analysed from SEM and EDS measurements. In this work, five systems were studied and are illustrated in Fig. 1. The interacting system corresponds to the NiCu/FeCo deposited samples, while the non-interacting is the stacking of the FeCo and NiCu single segments on top of each other. To improve the homogeneity of the magnetic segments, Au was initially grown for 7 min; and to protect the wires from oxidation, 1 min of Au was deposited at the end.

2.2. Characterization techniques

The morphology and chemical composition of the produced NW arrays were analysed by scanning electron microscopy (SEM, FEI Quanta 400FEG Field Emission) and energy dispersive X-ray spectroscopy (EDS). For the structural characterization, X-ray diffraction (XRD) data were acquired at room temperature using a *Rigaku SmartLab* diffractometer with Cu Kα radiation (1.5406 Å), 45 kV and 200 mA.

Major magnetic hysteresis loops were measured in a vibrating sample magnetometer (VSM, LakeShore Controller Model 7304) at room temperature by applying the magnetic field parallel and perpendicular to the NW's length. First-order reversal curves (FORCs) were acquired in an alternating gradient force magnetometer (AGFM, PMC MicroMag 2900 Series AGM) at room temperature with the magnetic field applied parallel to the NW's axis. Saturation fields (H_{Sat}) of 8, 2, 3, 4.5 and 5 kOe were used for the FeCo, NiCu, bi-segmented NiCu/FeCo (interacting), NiCu + FeCo (non-interacting) and NiCu/$[FeCo/Au]_3$ (multi-segmented) samples, respectively. 251 curves were extracted between $H_r^{min} = -H_{Sat}$ and $H_r^{max} = H_{Sat}$ for each sample, with an integration time of 300 ms and a waiting time of 1 s between each curve.

Ferromagnetic resonance (FMR) spectra were recorded at room temperature using a commercial electron spin resonance spectrometer (Bruker ELEXSYS E500) operating at 9.87 GHz (X-band). Measurements were performed in the range of angles $0^\circ \leqslant \theta_H \leq 90^\circ$ between the external magnetic field and the NWs' long axis, using a computer controlled goniometer.

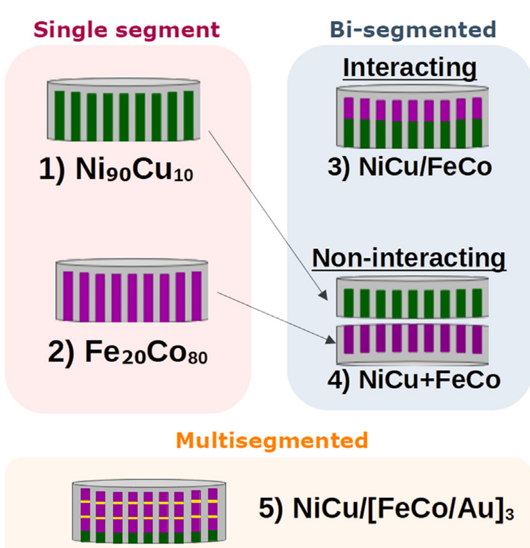

Fig. 1. Illustration of the samples studied in this work: (1) $Ni_{90}Cu_{10}$ and (2) $Fe_{20}Co_{80}$ single segments; (3) bi-segmented NiCu/FeCo NW arrays (interacting system); (4) non-interacting system composed of the superposition of the two different single segments; and (5) multi-segmented NiCu/$[FeCo/Au]_3$ NW arrays. (For simplicity, the samples' composition will not be written from this point.).

2.3. Micromagnetic simulations

The magnetic behaviour of the fabricated NW arrays was simulated using the Objected Oriented MicroMagnetic Framework (OOMMF) project [43]. Hexagonal arrays of 7 NWs with 48 nm in diameter and 100 nm of center-to-center distance were created with a cubic mesh size of $4 \times 4 \times 4$ nm^3. The $Ni_{90}Cu_{10}$ and $Fe_{20}Co_{80}$ saturation magnetization values used were $M_S^{NiCu} = 400 \times 10^3$ A/m and $M_S^{FeCo} = 1650 \times 10^3$ A/m, respectively, evaluated from the Slater-Pauling curve [44] and confirmed by the FMR measurements. The values for the stiffness constant ($A^{NiCu} = 8 \times 10^{-12}$ J/m and $A^{FeCo} = 28 \times 10^{-12}$ J/m) were estimated from the bulk Co, Fe, Ni values and the respective stoichiometries measured by EDS. The length of each magnetic segment was set to 148 nm in order to ensure large aspect ratios, following our previous work [33]. All simulations considered a stopping condition of $|dm/dt| = 1$ deg/ns and a damping factor of 0.015.

3. Results and Discussion

3.1. Bilayered NWs as Writing Elements

3.1.1. Morphological, chemical and structural characterization

SEM cross-sectional images of single and bilayered NW arrays are depicted in Figs. 2(a-c), where a good and close-to-homogeneous electrodeposition was reached for all samples. The NiCu and FeCo NW arrays presented a 6.0 ± 0.4 μm and 3.5 ± 0.2 μm NWs' length, respectively. Bilayered NWs were composed of 2.4 ± 0.2 μm and 4.4 ± 0.2 μm in length of NiCu and FeCo, respectively. This configuration aims at replicating a racetrack writing element made of a shorter soft layer coupled to a longer hard segment. Inset in Fig. 2(a) confirms the ordered hexagonal array of NWs with 47 ± 3 nm in diameter and center-to-center distances of 100 ± 5 nm.

The chemical composition was measured along the wires' length by EDS (Fig. 2(d)). The desired composition of $88 \pm 2\%$ Ni and $12 \pm 2\%$ Cu in NiCu alloys, and $19 \pm 2\%$ Fe and $81 \pm 2\%$ Co in the FeCo segments has been obtained, presenting a uniform distribution for all samples.

Finally, the crystallographic structure was measured by XRD and identified using the ICSD database. The resulting pattern (not shown) revealed the formation of a face centered cubic (fcc) structure for both FeCo and NiCu arrays with the (110) and (111) textures, respectively, in agreement with previous reports [39,37]. According to Zhang et al. [45] duplication of the structure of the piling layer favours good connection and therefore a smooth interface between the different layers.

3.1.2. Magnetic hysteresis loops

Magnetic hysteresis loops were measured at room temperature with the magnetic field applied parallel and perpendicular to the NWs' axis (Figs. 3(a-c)). All samples exhibited higher coercivities and remanence values when applying the magnetic field parallel to the wire axis, illustrating a magnetization easy axis lying along

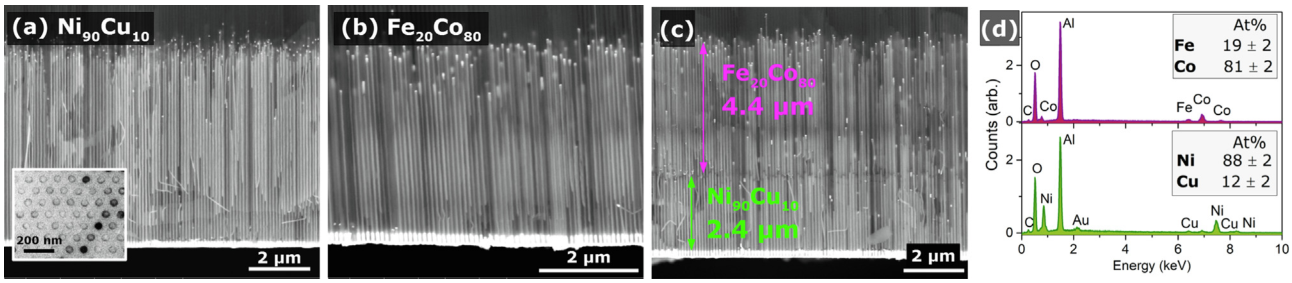

Fig. 2. Cross-sectional SEM images of (a) $Ni_{90}Cu_{10}$, (b) $Fe_{20}Co_{80}$, and (c) bilayered $Ni_{90}Cu_{10}/Fe_{20}Co_{80}$ coupled NW arrays, with the depicted compositions as obtained through EDS analysis, shown in (d). Inset in (a) shows a bottom view of the filled template after chemical etching of the Au contact layer.

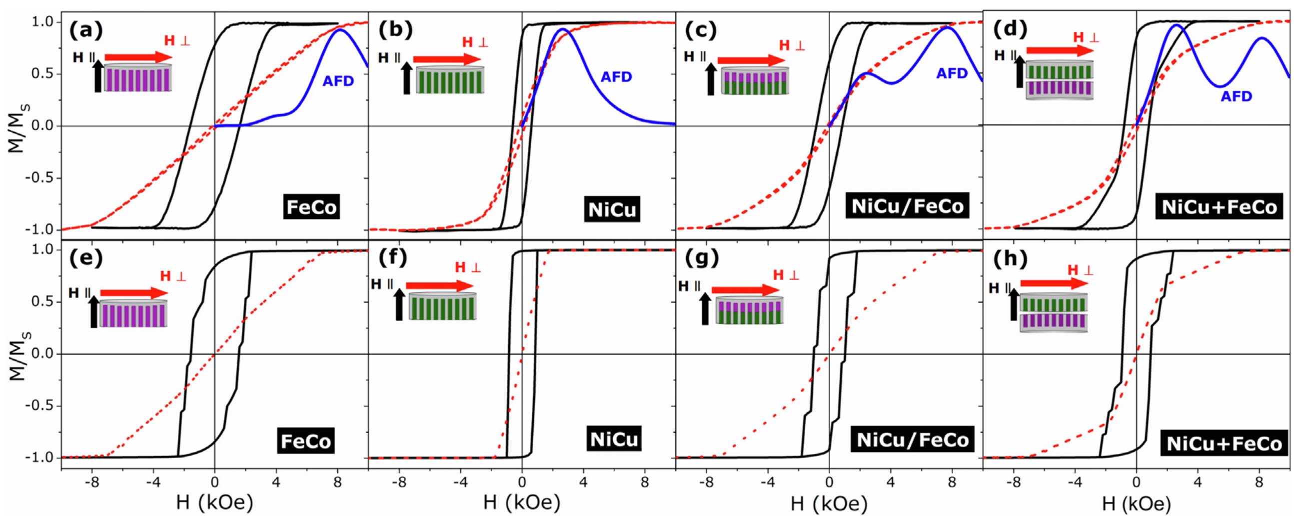

Fig. 3. Normalized magnetic hysteresis loops (a-d) experimentally measured and (e-g) simulated by applying the magnetic field parallel (black solid line) and perpendicular (red dashed line) to the NWs' axis for the (a,e) $Fe_{20}Co_{80}$, (b,f) $Ni_{90}Cu_{10}$, (c,g) interacting NiCu/FeCo and (d) non-interacting NiCu + FeCo samples. The hysteresis loop in (h) corresponds to the weighted superposition of the simulated loops in (e) and (f) as explained in the main text. The estimated normalized anisotropy field distributions (AFD) are represented by a blue solid line in (a-d).

the wire length, as expected. This is ascribed to the strong shape anisotropy provided by the high aspect ratios of the wires (length $\gg$ diameter).

$Fe_{20}Co_{80}$ NW arrays presented the highest parallel coercivity (Fig. 3(a)), reaching $\sim$ 1.6 kOe, in agreement with previous reports for NW arrays with 50 nm in diameter [36,37]. As for the $Ni_{90}Cu_{10}$ NWs, the lowest parallel coercive field was observed ($\sim$ 0.61 kOe), while keeping normalized remanence values close to 0.9 (Fig. 3(b)). These results confirm the successful fabrication of hard and soft magnets composed of $Fe_{20}Co_{80}$ and $Ni_{90}Cu_{10}$ NW arrays, respectively.

By producing a bilayered NiCu/FeCo NW array (interacting system), the coupling between the soft and hard magnetic layers leads to a reduction of the parallel coercivity and normalized remanence to around 0.85 kOe and 0.6, respectively (Fig. 3(c)). This supports the feasibility of creating a magnetic writing element along a racetrack wire composed of an interacting soft/hard magnetic system.

To study the importance of the interface between the hard and soft magnetic layers, the FeCo and NiCu NW array samples were stacked and measured together. This allowed recreating a non-interacting bilayered magnetic system where the FeCo and NiCu NWs were not in contact (NiCu + FeCo system). To ensure an equivalent magnetic signal from each material, and since $M_S^{FeCo} \approx 4 \times M_S^{NiCu}$, the NiCu magnetic volume was set to approximately 4 times the total FeCo magnetic volume. For that, the area of the FeCo sample was reduced to half the area of the NiCu sample (note that the length of the FeCo NWs is almost half the length of the NiCu NWs). Fig. 3(d) shows the magnetic hysteresis loops obtained, where a parallel coercivity reduction (to around 0.85 kOe) can be observed, similarly to the interacting sample. However, in this non-interacting system, the shapes of the hysteresis loops clearly evidence the existence of a two-step reversal process [27,46–48]. At low applied magnetic fields, the high differential susceptibility suggests the reversal of the soft NiCu segment; while at higher magnetic fields, the susceptibility takes a smaller value, denoting the reversal of the hard FeCo segment.

To evaluate the magnetic reversal processes of the NW arrays, micromagnetic simulations were carried out for the FeCo, NiCu and interacting NiCu/FeCo samples. Good agreement can be observed between the simulated and experimentally measured loops (Figs. 3(a-c) and (e-g)), in which large (small) parallel coercive field values can be found for the FeCo (NiCu) NW arrays. Similarly, the reduction of the parallel coercive field for the bilayered NiCu/FeCo interacting system was also reproduced, confirming once more its feasibility to be used as a writing element.

For the non-interacting system, a weighted superposition of the magnetic loops of FeCo and NiCu single arrays was performed. To better replicate the experimentally measured loops, $(M/M_S)^{(NiCu+FeCo)} = 0.5(M/M_S)^{NiCu} + 0.5(M/M_S)^{FeCo}$. Again, good agreement was obtained between the calculated (Fig. 3)) and the measured (Fig. 3(d)) magnetic loops, illustrating a two-step reversal process along both directions. At low applied fields, smaller parallel coercivities and higher differential susceptibilities were obtained, associated with the reversal of the soft NiCu NWs. While, at higher fields, a broadening of the parallel hysteresis loops occurred together with a decrease in susceptibility, ascribed to the reversal of the harder FeCo NWs.

3.1.3. Magnetic anisotropy

Elongated ferromagnetic NWs with high uniaxial anisotropy are known to exhibit narrow anisotropy field distributions (AFD) along the hard magnetization axis, centered at the effective anisotropy field (H_{eff}) [49,50,27,51]. Normalized AFD curves, obtained from $\sigma(H) = -H(\mathrm{d}^2M/\mathrm{d}H^2)$, are depicted in blue in Figs. 3(a-d), and the collected H_{eff}^{AFD} values summarized in Table 1. The higher (lower) H_{eff} values obtained for the FeCo (NiCu) NW segments revealed once more the hard (soft) magnetic behavior of each material. In the FeCo AFD curve, an additional small bump is also visible at around 3.8 kOe, which might be arising from a possible two-step magnetization reversal process, as will be further explored through micromagnetic simulation analysis.

In the bilayered (interacting and non-interacting) systems, the AFD profiles present two intense peaks corresponding to the two different magnetic segments' anisotropy. As illustrated in Fig. 3 and summarized in Table 1, H_{eff}^{AFD} for the NiCu layer remains almost unchanged (2.6 kOe for single arrays and 2.46 kOe for bilayered). Whereas for the FeCo, it shifts towards lower field values ($\sim$ 7.65 kOe) when coupled to the NiCu layer and remains the same ($\sim$ 8.1 kOe) for the non-interacting system, evidencing the strong magnetic interactions present at the hard/soft interface.

FMR measurements were also used to extract the H_{eff} values for all samples following the procedures previously reported [52–55]. Angular dependence of the resonance field was fitted using simplified Kittel equations with only two fitting parameters: H_{eff}^{FMR} and the gyromagnetic ratio γ (see Ref. [56] for more details).

For the array of NiCu NWs, a single resonance peak was observed in the whole range of applied field angles (θ_H). The best fit was obtained for $H_{eff}^{FMR} = 1.65$ kOe and $\gamma/2\pi = 3.1$ MHz/Oe, reasonably close to the reference value 3.12 MHz/Oe for the bulk Ni [57]. Using the modified Kittel's equation for a columnar granules and the parameters from the SEM images, M_S of NiCu was determined to be 400×10^3 A/m (value used in the micromagnetic simulations).

The situation for FeCo NWs was quite different. Due to the much higher M_S of FeCo, it was impossible to observe the FMR spectra in the whole θ_H range, as the resonance field for $\theta_H = 0^\circ$ (parallel to the wires' axis) moves to negative values. Thus, H_{eff}^{FMR} was extracted from detailed measurements around $\theta_H = 90^\circ$ (perpendicular to the wires' axis). For simplicity, $\gamma/2\pi$ was fixed at the bulk Co value of 3.14 MHz/Oe and H_{eff}^{FMR} was found to be 7.15 kOe. Using the same NW array diameter and center-to-center distance as for NiCu NWs, we obtained $M_S = 1650 \times 10^3$ A/m (value used in the micromagnetic simulations). Although smaller H_{eff}^{FMR} values were obtained in comparison to the AFD measurements (see Table 1), the soft and hard magnetic behavior of NiCu and FeCo, respectively, was still present.

For the bilayered NW arrays, two FMR peaks were observed in the vicinity of $\theta_H = 90^\circ$ and only one at $\theta_H = 0^\circ$. For the non-interacting system, since the arrays are physically separated, the values of H_{eff}^{FMR} are very similar (within the accuracy range) to the ones of individual NW arrays (1.6 and 7.15 kOe for the NiCu and FeCo uncoupled segments, respectively). The significant change in the H_{eff}^{FMR} values occurs for the interacting system, where 0.55 and 7.0 kOe were obtained for the NiCu and FeCo interacting segments, respectively. The simple Kittel model should not be used to measure directly effective anisotropy in interacting multi-segmented NWs due to the dynamic coupling between different magnetic materials. Our results thus show that there is a strong interface coupling between the soft and hard segments, thus hindering the correct estimation of the H_{eff}^{FMR} values. Nonetheless, it should be highlighted that the FMR results present higher accuracy than the AFD method. This is due to the high dipolar interactions that reduce the single domain character of the NWs required for a more reliable AFD analysis [49].

3.1.4. Magnetic interactions

To understand the role of each magnetic layer in the writing process of a racetrack memory device, FORCs [$M(H, H_r)$]) were measured for all samples with the magnetic field applied parallel to the wires' long axis (insets in Fig. 4). The FORC diagrams, represented as color contour plots in Fig. 4, were obtained by calculating the second-order mixed derivative of $M(H, H_r)$ [27]. From the FORC diagram one can extract the switching and interaction field distributions by analysing the profile distribution width along the $H_c = (H - H_r)/2$ and $H_u = -(H + H_r)/2$ axis, respectively [58,59], and the coercive field (H_c^{FORC}) as the maximum of the switching field distribution profile.

For the FeCo and NiCu single segments, the FORC diagrams illustrate a "T-shape" profile (Figs. 4(a) and (b)), typical of ferromagnetic NW arrays with negative mean interaction fields [60,61]. However, much stronger magnetic interactions (larger span along the H_u axis) and higher coercivities ($\sim$ 1.61 kOe) can be found for the FeCo NW arrays when compared to NiCu ($\sim$ 0.53 kOe), in good agreement with the H_c values obtained from the parallel hysteresis loops (see Table 1). These results evidence once more that the FeCo NWs are magnetically harder than the NiCu NWs, with stronger magnetostatic interactions due to the higher saturation magnetization of FeCo (1650×10^3 A/m) with respect to NiCu (400×10^3 A/m).

The FORC diagram of the bilayered non-interacting system (Fig. 4(d)) illustrated a simple superposition of the individual FORC diagrams of NiCu and FeCo NW arrays (Figs. 4(a) and (b)). Similar results were reported for decoupled Ni/Co bi-magnetic systems,

Table 1
Summary of selected parameters extracted from the magnetic characterization techniques for the single, bilayered and multilayered NW arrays, namely: parallel coercive fields obtained from the hysteresis loops (H_c^{loop}) and from the FORC diagrams (H_c^{FORC}); and the effective anisotropy fields acquired from the AFD curves (H_{eff}^{AFD}) and FMR analysis (H_{eff}^{FMR}). Measurement uncertainties correspond to approximately 5% of the respective estimated field values.

Sample	Segment	H_c^{loop} (kOe)	H_c^{FORC} (kOe)	H_{eff}^{AFD} (kOe)	H_{eff}^{FMR} (kOe)
NiCu		0.61	0.53	2.60	1.65
FeCo		1.60	1.61	8.10	7.15
Interacting	NiCu	0.85	0.57	2.46	0.55
	FeCo		0.85	7.65	7.00
Non-interacting	NiCu	0.85	0.57	2.46	1.60
	FeCo		1.61	8.14	7.15
Multi-segmented	NiCu	1.00	0.83	2.00	0.55
	FeCo		1.15	8.00	7.05

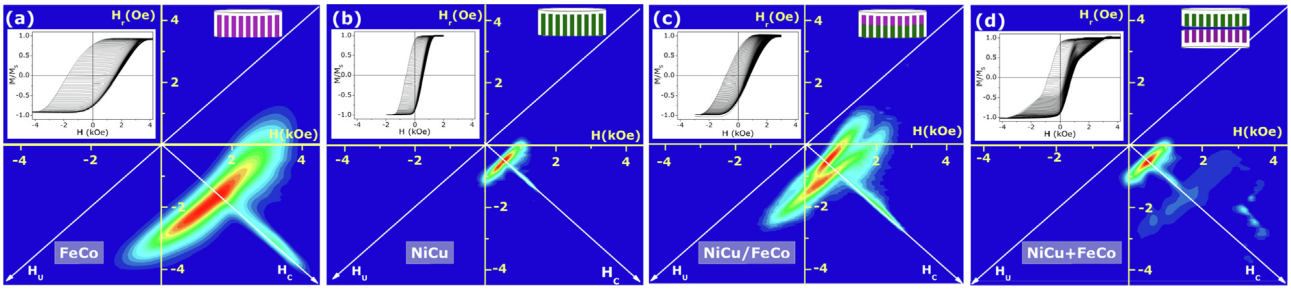

Fig. 4. First order reversal curves (insets) and respective FORC diagrams measured by applying the magnetic field parallel to the NWs' long axis for (a) FeCo, (b) NiCu, (c) bi-segmented NiCu/FeCo (interacting) and (d) non-interacting NiCu + FeCo NW arrays.

where the soft segments dominated the FORC diagram while the hard segments appeared as a "shadow" at higher H_c fields [27]. The coercive field values extracted from the FORC diagram were similar to the ones obtained for the individual arrays (see Table 1).

Finally, for the NiCu/FeCo bilayered interacting NW array, a complex FORC diagram was obtained (Fig. 4(c)), illustrating a two-step magnetization reversal fingerprint as previously reported for nanostructured hard/soft coupled systems [27,47,62,63]. This effect results from the large difference between the hard and soft coercive fields ($H_c^{FeCo} \approx 3H_c^{NiCu}$). The two branches in this FORC diagram thus demonstrate that the switching of the soft segments (at ~ 0.57 kOe) induced the reversal of the FeCo hard segments at much lower coercive fields (~ 0.85 instead of ~ 1.61 kOe). These results indicate that although a two-step reversal process occurs, the switching field of the hard segments is reduced to almost half its value due to the strong interactions at the hard/soft magnetic interface, and thus a writing element of such composition is still feasible.

3.1.5. Magnetic reversal modes

Given the FORC results, a more detailed study on the magnetization reversal processes in individual and bilayered interacting NW arrays was performed. Parallel magnetic hysteresis loops were simulated and the respective spin configurations analysed during the reversal process (Fig. 5).

For the array with 7 NiCu NWs, complete reversal occurred at applied field values between 0.8 and 1.0 kOe. First, two transverse domain walls (T-DWs) were nucleated at the extremities of each NW. These then propagated along the wire length transforming into asymmetric T-DWs (also known as vertical vortices) during reversal [33], as depicted in Fig. 5(a).

Distinctly, for the FeCo array, reversal seemed to have occurred by a two-step process (Fig. 5(b)). Already at remanence (zero applied field), two vortex DWs (V-DWs) were nucleated at both ends of all NWs. However, only at an applied field value of 0.8 kOe, one of the V-DWs of the central NW started to evolve into one skyrmion tube with increasing length. Complete reversal of the central wire then occurred by the creation of one hedgehog-antihedghog pair (or Block point) at the skyrmion tube core that rapidly moved along the wire [29]. At higher applied field values (between 1.6 and 2.4 kOe), the external NWs completed their reversal by forming asymmetric T-DWs (vertical vortices).

Finally, in the coupled system, a multi-step reversal process occurred. The interface between NiCu and FeCo appears to facilitate the propagation of V-DWs and difficult the nucleation of T-DWs in NiCu (and also the propagation of T-DWs across the interface, as will be seen later). When analysing the separate FeCo and NiCu segments, the nucleation of V-DWs in FeCo NW arrays was found to occur at lower applied fields (zero) than the nucleation of T-DWs in NiCu NW arrays (0.8 kOe). This effect induced the reversal of the coupled system at 0.2 kOe by the nucleation of a V-DW at the central FeCo segment (see upper time snapshots in Fig. 5(c)). During reversal, the V-DW increased its size forming a skyrmion tube that rapidly reversed the magnetization of the FeCo

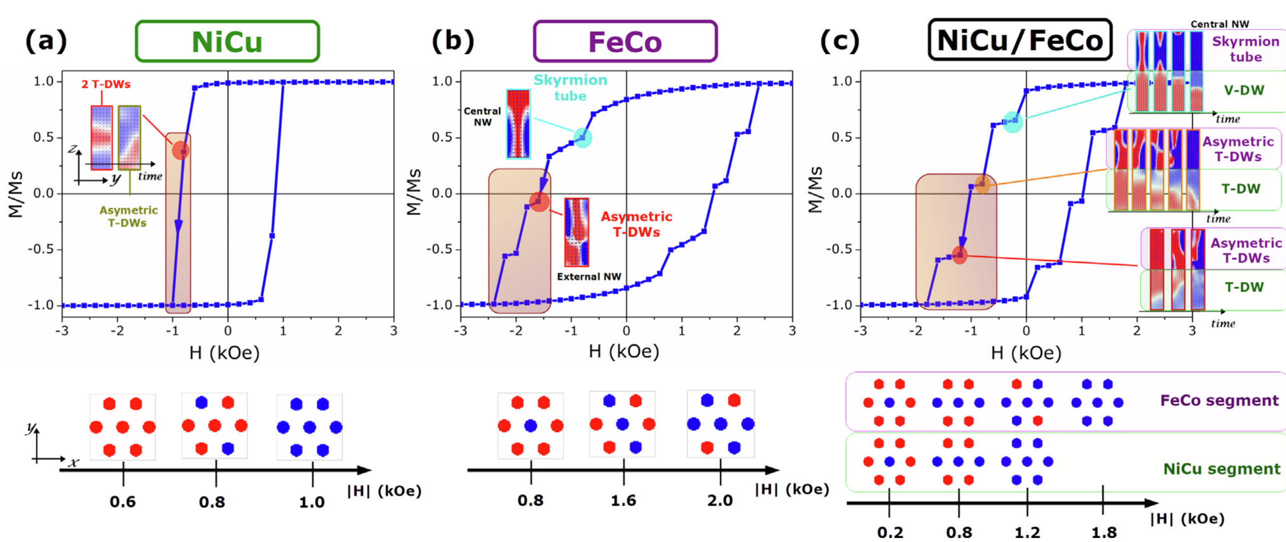

Fig. 5. Simulated parallel hysteresis loops with selected 2D cross-sectional time snapshots along the *yz*-plane, and summarized timeline with the respective *xy*-plane 2D cross-sectional views of the NW arrays after different applied fields for (a) NiCu, (b) FeCo and (c) coupled NiCu/FeCo systems. All 2D cross-sections were taken at the center of the wires. The color scale is red ($M_z/M_S = 1$), white ($M_z/M_S = 0$) and blue ($M_z/M_S = -1$), where $M_S = M_S^{FeCo}/3.3 = M_S^{NiCu}/0.8 = 500 \times 10^3$ A/m.

segment and transformed into a V-DW at the NiCu/FeCo interface. This V-DW then propagated towards the external end of the central NiCu segment changing chirality from clockwise to counter-clockwise several times during reversal.

At 0.8 kOe two external NWs completed their reversal. First, the V-DWs formed at the FeCo segments' extremities started propagating forming asymmetric T-DWs in the FeCo region (see corresponding time snapshots in Fig. 5(c)). These induced the nucleation of a T-DW at the FeCo/NiCu interface, which then propagated along each NiCu segment, completing their reversal.

Only at 1.2 kOe the nucleation and propagation of T-DWs in the external NiCu segments became more favourable than the propagation of the (nucleated) V-DWs in the external FeCo segments (that would occur at 1.6 kOe if decoupled). Therefore, at 1.2 kOe nucleation and propagation of T-DWs in the remaining 4 external NiCu segments occurred. Two of these DWs then induced the reversal of the respective coupled FeCo segments at lower applied fields, forming asymmetric T-DWs (see respective time snapshots in the hysteresis loop of Fig. 5(c)). However, as can be seen in the timeline in Fig. 5(c), the other two T-DWs got pinned at the NiCu/FeCo interface, and could only be depinned at 1.8 kOe, completing the reversal process of the coupled system.

In summary, micromagnetic simulations confirmed the multi-step reversal process previously depicted in the FORC diagram of the coupled system. In addition, the soft/hard magnetic interface was found to influence the type of DW nucleated as well as the propagation, pinning and depinning processes of the different DW-types across it. Nonetheless, even though a few DWs got pinned at the soft/hard interface, the overall magnetic field needed to complete the reversal of the wires was smaller in the coupled system (1.8 kOe) than in the hard FeCo NW array (2.4 kOe), confirming its feasibility as a writing element.

3.2. Multisegmented NWs as Racetrack Memories

From the results discussed above, it has been shown that the NiCu/FeCo bi-magnetic segment can be used as the writing component of a 3D racetrack memory device [15,25]. To further evaluate the effect of assembling the writing section into a racetrack ferromagnetic NW, two FeCo magnetic storage segments were grown on top of the writing NiCu/FeCo system. Thin Au layers ($\sim$ 20 nm) were used to separate the FeCo hard segments thus obtaining a multi-segmented NW array similar to the racetrack NWs previously proposed and simulated by Rial and Proenca [15].

Fig. 6(a) shows the multi-segmented NiCu/$[FeCo/Au]_3$ NW array successfully produced, with NiCu and FeCo segments' length of $\sim$ 1 and $\sim$ 4μm, respectively, and 20 nm non-magnetic Au constraints between the FeCo storage segments, as intended. The choice of Au as the non-magnetic constraint was due to its better visualization in the SEM images; however, according to simulations, any non-magnetic spacing layer can be used in these systems [15].

The magnetic hysteresis loops presented in Fig. 6(b), show again higher coercivities and remanence values along the parallel direction, evidencing a dominant shape anisotropy effect. Although the amount of FeCo is much higher than the NiCu one, a reduced parallel coercivity is again observed when compared to single FeCo NW arrays (from 1.6 to 1.0 kOe). Similar to the behavior of the bilayered NiCu/FeCo interacting system, the strong magnetic coupling between the hard and soft layers reduces the overall coercivity of the multilayered sample (see Table 1). These observations suggest that, even with three hard FeCo layers, the soft NiCu segment is still able to induce the switching of the writing element at lower applied fields. The chemical constraints (20 nm-thick Au layers) between the hard FeCo segments could then be used as DW pinning sites, and the magnetic domains (information bits) be pushed into the storage sections and along the racetrack multi-segmented NW using short pulses of spin-polarized current [15,28,64,17]. Magnetoresistance measurements have already revealed the pinning and depinning processes using current pulses through the multi-segmented wires (following the experimental set-up described by Proenca et al. [65]). However, these are still under development and the results will be addressed in a future work.

The magnetic anisotropy field of the multi-segmented NW array was also studied by both FMR and calculations of the AFD (blue curve in Fig. 6(b)). The H_{eff} values extracted from the FMR measurements are very similar to the ones obtained for the bilayered coupled system (0.55 and 7.05 kOe for the NiCu and FeCo segments, respectively). These results demonstrated once more the strong magnetic coupling effect present at the soft/hard interface, which hindered the correct estimation of the H_{eff} values from FMR data.

Analysing the AFD profile in Fig. 6(b), well-pronounced peak centered at 8.0 kOe can be observed for the FeCo segments and a very small peak at 2.0 kOe for NiCu. In this system, both H_{eff} values were reduced, indicating that, in one hand, the magnetic hard/soft coupling at the interface is still strong enough to reduce the H_{eff} of the FeCo segments, but, on the other hand, the increased amount of FeCo in the overall sample is pushing the H_{eff} of the NiCu segments to smaller values due to the stronger interactions between neighbouring wires. This increase in the magnetostatic interactions can also be seen by the reduction of the remanence values in the major parallel hysteresis loop (Fig. 6)) and in the following analysis of the FORC diagram.

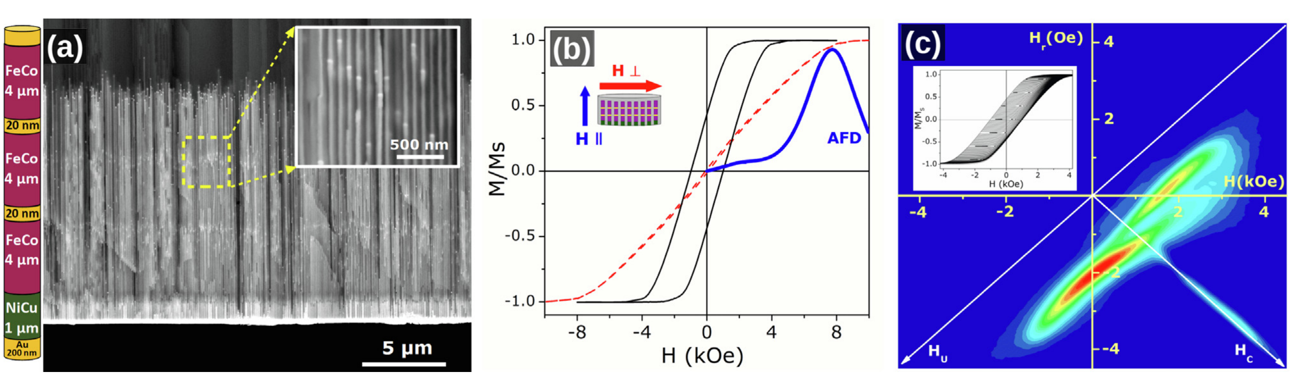

Fig. 6. (a) SEM cross-sectional image and schematic illustration of the multi-segmented NiCu/$[FeCo/Au]_3$ NWs produced. Inset shows a magnified view evidencing the 20 nm-thick Au layers (brighter segments). (b) Normalized magnetic hysteresis loops of the multi-segmented NW array measured by applying the magnetic field parallel (black solid line) and perpendicular (red dashed line) to the NWs' long axis. The estimated normalized anisotropy field distribution (AFD) is represented by a blue solid line. (c) FORCs (inset) and FORC diagram of the multi-segmented sample measured with the applied field parallel to the NWs' length.

FORC measurements were also performed for the multi-segmented system when applying the magnetic field parallel to the NWs' axis. Fig. 6(c) shows the FORCs (inset) and respective FORC diagram obtained, illustrating a two-step reversal process similar to the one observed in the bilayered coupled system (Fig. 4(c)). In this case, the interaction field (span along the H_u axis) is much higher for the branch at higher coercivities, indicating much stronger interactions between the FeCo segments. This can be ascribed to the higher amount of FeCo present in this sample, which increased the magnetic interactions between neighbouring wires, as also observed when analysing the $M(H)$ and AFD profile. From the two peaks in the FORC diagram, two coercive field values were extracted: around 0.83 kOe for the soft segments and 1.15 kOe for the harder ones (see Table 1). Again, a reduction of the FeCo H_c value occurs (from 1.61 to 1.15 kOe), evidencing the strong coupling between the soft and hard segments, which promoted the reversal of the writing element at lower applied fields, even when attached to a racetrack storage NW. However, the reversal of the NiCu soft segment occurred at higher fields than in the single or bilayered systems (increased from 0.53 to 0.83 kOe). This can be associated with the increase of magnetic FeCo hard segments along the wires, which interact with the soft segments pushing the NiCu coercivity to higher values.

To summarize, Fig. 7 shows a comparative analysis of the parallel ($H_c^{\parallel}$) and perpendicular ($H_c^{\perp}$) coercive values for the single, bilayered (interacting) and multilayered systems. At a first glance, $H_c^{\parallel}$ is always higher than $H_c^{\perp}$, evidencing the uniaxial anisotropy typically present in elongated magnetic NWs. Regarding the $H_c^{\parallel}$ values, the FORC method provided an additional degree of magnetic characterization by distinguishing the parallel coercivities of each magnetic element (NiCu soft and FeCo hard segments) present in the bi- and multi-segmented arrays. Finally, the reduction of $H_c^{\parallel}$ for the mixed systems revealed the importance of interlayer interactions. The slightly higher value for the multi-segmented NWs was related to the larger amount of hard segments in comparison to the bilayered (interacting) NWs. Nonetheless, a successful reduction of $H_c^{\parallel}$ was obtained when introducing a soft/hard interface along the racetrack NW, further proving the feasibility of integrating an in-line writing element.

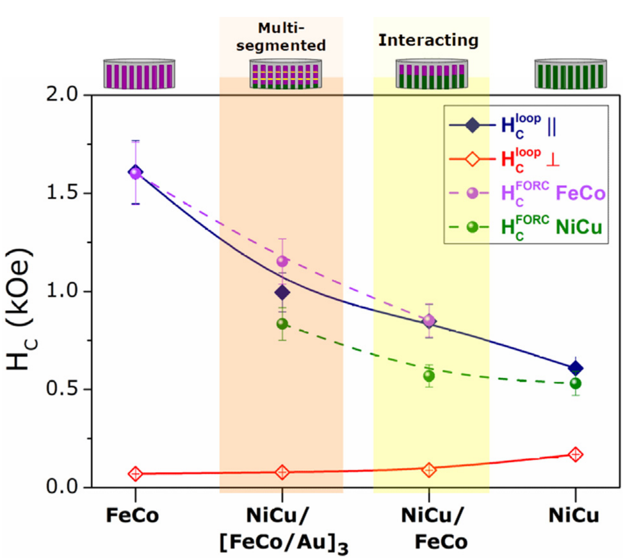

Fig. 7. Coercive field (H_c) values obtained for the FeCo, NiCu/[FeCo/Au]$_3$ (multi-segmented), NiCu/FeCo (interacting) and NiCu NW arrays when applying the field parallel (‖) and perpendicular (⊥) to the NWs' long axis. The values were extracted from the major hysteresis loops (H_c^{loop}) and from the parallel FORC diagram (H_c^{FORC}) and are summarized in Table 1. Lines are gu.ides to the eye.

Furthermore, bilayered NWs can also be fabricated by changing the diameter of each segment or their crystallographic properties, as chemical composition, morphology and crystallographic structure are know to affect the magnetic behavior of cylindrical NWs [15,66–68,40]. In addition, considering practical applications, smaller track sizes (diameter and length) are preferable for reduced devices, which can be easily achieved through template-assisted electrodeposition methods[1]. This work thus provides an important pathway to implement a variety of adjustable bilayered writing elements in 3D racetrack memory devices, hence increasing their functionality and applicability.

4. Conclusions

Interacting bilayered magnetic systems composed of NiCu/FeCo NW arrays have been demonstrated as possible candidates to be applied as writing components in 3D racetrack memory devices. Morphological, chemical and structural characterization revealed the formation of single, bi- and multi-segmented NW arrays with tuned dimensions and uniform compositions by template-assisted DC electrodeposition in nanoporous alumina templates.

Magnetic hysteresis loops, FMR measurements and FORC diagram analysis confirmed the hard and soft magnetic properties of the FeCo and NiCu single arrays, respectively. In the interacting NiCu/FeCo bi- and multi-segmented systems, a significant reduction of the parallel coercive field occurred, while keeping the magnetization easy axis lying parallel to the wires' long axis. FORC diagrams also demonstrated a two-step reversal process in both bi- and multi-segmented NWs, illustrating a FORC fingerprint typically present in soft/hard magnetic interacting bilayered systems. Using micromagnetic simulations we were also able to confirm and visualize such a multi-step reversal process, which revealed the importance of the strong interactions present at the soft/hard interface.

This work provides a new pathway for the fabrication of 3D racetrack memory devices with incorporated writing heads along the track. The writing elements were made of soft/hard materials with different chemical compositions. Other parameters (diameter, length, crystallographic structure) can also be tuned to create a wider variety of writing sections, thus increasing the applicability of such devices.

5. Data Availability

All data generated or analysed during this study are included in this published article.

Declaration of Competing Interest

The authors declare that they have no known competing financial interests or personal relationships that could have appeared to influence the work reported in this paper.

Acknowledgement

C.T.S. and S.A.B. thank the Portuguese *Fundação para a Ciência e Tecnologia* (FCT) for financial support through the *Investigador FCT* program (Contract No. IF/01159/2015 and project EXPL/IF/00541/2015, respectively) and Atracción de Talento (CAM), Ref. 2020-T1/IND-19889. V.O.G. is grateful for the support from grant 02.2020/0261 provided by National Research Foundation of Ukraine. The authors acknowledge funding from the European Union's Horizon 2020 research and innovation program under the Marie Sklodowska-Curie Grant Agreement No. 734801, from FCT and COMPETE 2020 (FEDER) under the projects POCI-01–0145-FEDER-028676, POCI-01–0145-FEDER-031302, POCI-01–0145-FEDER-032257, POCI-01–0145-FEDER-032527 and UIDB/04968/2020, and from the Spanish *Ministerio de Ciencia e Innovación* under the project PID2020-117024 GB-C42. This work was also funded by the Network of Extreme Conditions Laboratories (NECL) under the project NORTE-01–0145-FEDER-022096. This work has also made use of the Spanish ICTS Network MICRONANOFABS.

References

[1] C. Sousa, D. Leitao, M. Proenca, J. Ventura, A. Pereira, J. Araujo, Appl. Phys. Rev. 1 (2014) 031102.
[2] E. Bertero, C.V. Manzano, G. Bürki, L. Philippe, Mater. Des. 190 (2020) 108559.
[3] D.S. Wang, A. Mukhtar, K.M. Wu, L. Gu, X. Cao, Materials 12 (2019) 3908.
[4] M. Vazquez (Ed.), Magnetic Nano- and Microwires: Design, Synthesis, Properties and Applications, 2nd ed., Woodhead Publishing, 2020.
[5] M. Vazquez, J. Magn. Magn. Mater. 543 (2022) 168634.
[6] S.S. Parkin, M. Hayashi, L. Thomas, Science 320 (2008) 190–194.
[7] L. Thomas, R. Moriya, C. Rettner, S.S. Parkin, Science 330 (2010) 1810–1813.
[8] Y.P. Ivanov, A. Chuvilin, S. Lopatin, H. Mohammed, J. Kosel, ACS Applied Materials & Interfaces 9 (2017) 16741–16744.
[9] L. Thomas, S.-H. Yang, K.-S. Ryu, B. Hughes, C. Rettner, D.-S. Wang, C.-H. Tsai, K.-H. Shen, S.S. Parkin, Racetrack memory: a high-performance, low-cost, non-volatile memory based on magnetic domain walls, International Electron Devices Meeting. 2011 (2011) 24–32.
[10] E. Ramos, C. López, J. Akerman, M. Muñoz, J.L. Prieto, Physical Review B 91 (2015) 214404.
[11] M. Yan, A. Kákay, S. Gliga, R. Hertel, Phys. Rev. Lett. 104 (2010) 057201.
[12] D.-S. Wang, A. Mukhtar, K.-M. Wu, L. Gu, X. Cao, Materials 12 (2019) 3908.
[13] M.R.Z. Kouhpanji et al., IEEE Trans. Magn. (2022).
[14] T. Da Câmara Santa Clara Gomes, N. Marchal, F.A. Araujo, L. Piraux, J. Phys. D: Appl. Phys. 55 (2022) 223001.
[15] J. Rial, M.P. Proenca, Nanomaterials 10 (2020) 2403.
[16] S. Ruiz-Gómez, M. Foerster, L. Aballe, M.P. Proenca, I. Lucas, J.L. Prieto, A. Mascaraque, J. de la Figuera, A. Quesada, L. Pérez, Scientific Reports 8 (2018) 16695.
[17] M. Schöbitz, S. Finizio, A. De Riz, J. Hurst, C. Thirion, D. Gusakova, J.C. Toussaint, J. Bachmann, J. Raabe, O. Fruchart, Appl. Phys. Lett. 118 (2021) 172411.
[18] E. Berganza, M. Jaafar, C. Bran, J.A. Fernández-Roldán, O. Chubykalo-Fesenko, M. Vázquez, A. Asenjo, Scientific Reports 7 (2017) 11576.
[19] D. Reyes, N. Biziere, B. Warot-Fonrose, T. Wade, C. Gatel, Nano Lett. 16 (2016) 1230–1236.
[20] B. Ozkale, N. Shamsudhin, G. Chatzipirpiridis, M. Hoop, F. Gramm, X. Chen, X. Martí, J. Sort, E. Pellicer, S. Pané, ACS Applied Materials & Interfaces 7 (2015) 7389–7396.
[21] C. Bran, E. Saugar, J.A. Fernandez-Roldan, R.P. del Real, A. Asenjo, L. Aballe, M. Foerster, A. Fraile Rodríguez, E.M. Palmero, M. Vazquez, O. Chubykalo-Fesenko, Nanoscale 13 (2021) 12587–12593.
[22] S. Moraes, D. Navas, F. Béron, M.P. Proenca, K.R. Pirota, C.T. Sousa, J.P. Araújo, Nanomaterials 8 (2018) 490.
[23] A. Ramazani, M. Ghaffari, M.A. Kashi, F. Kheiry, F. Eghbal, J. Phys. D: Appl. Phys. 47 (2014) 355003.
[24] S. Caspani, S. Moraes, D. Navas, M.P. Proenca, R. Magalhães, C. Nunes, J.P. Araújo, C.T. Sousa, Nanomaterials 11 (2021) 2729.
[25] Y.P. Ivanov, A. Chuvilin, S. Lopatin, J. Kosel, ACS Nano 10 (2016) 5326–5332.
[26] A. Núñez, L. Pérez, M. Abuín, J.P. Araujo, M.P. Proenca, J. Phys. D: Appl. Phys. 50 (2017) 155003.
[27] J. García Fernández, V. Vega Martínez, A. Thomas, V.M. De la Prida Pidal, K. Nielsch, Nanomaterials 8 (2018) 548.
[28] J.A. Moreno, H. Mohammed, J. Kosel, J. Magn. Magn. Mater. 484 (2019) 110–113.
[29] J.A. Fernández-Roldán, Y.P. Ivanov, O. Chubykalo-Fesenko, Magnetic Nano-and Microwires, Elsevier, 2020, pp. 403–426.
[30] M. Susano, M.P. Proenca, S. Moraes, C.T. Sousa, J.P. Araújo, Nanotechnology 27 (2016) 335301.
[31] H. Yao, L. Xie, Y. Cheng, J. Duan, Y. Chen, S. Lyu, Y. Sun, J. Liu, Mater. Des. 123 (2017) 165–173.
[32] T. Hasegawa, S. Kanatani, M. Kazaana, K. Takahashi, K. Kumagai, M. Hirao, S. Ishio, Scientific Reports 7 (2017) 13215.
[33] M.P. Proenca, J. Rial, J.P. Araujo, C.T. Sousa, Scientific Reports 11 (2021) 10100.
[34] K. Gandha, P. Tsai, G. Chaubey, N. Poudyal, K. Elkins, J. Cui, J.P. Liu, Nanotechnology 26 (2015) 075601.
[35] D. Qin, L. Cao, Q. Sun, Y. Huang, H. Li, Chem. Phys. Lett. 358 (2002) 484–488.
[36] D.-H. Qin, Y. Peng, L. Cao, H.-L. Li, Chem. Phys. Lett. 374 (2003) 661–666.
[37] G. Yue, X. Wang, L. Wang, P. Chang, R. Wen, Y. Chen, D. Peng, Electrochim. Acta 54 (2009) 6543–6547.
[38] C. Bran, E.M. Palmero, Z.-A. Li, R.P. del Real, M. Spasova, M. Farle, M. Vazquez, J. Phys. D: Appl. Phys. 48 (2015) 145304.
[39] E.M. Palmero, C. Bran, R. del Real, C. Magén, M. Vázquez, J. Appl. Phys. 116 (2014) 033908.
[40] E.M. Palmero, M. Méndez, S. González, C. Bran, V. Vega, M. Vázquez, V.M. Prida, Nano Research 12 (2019) 1547–1553.
[41] J. Marqués-Marchán, J.A. Fernandez-Roldan, C. Bran, R. Puttock, C. Barton, J.A. Moreno, J. Kosel, M. Vazquez, O. Kazakova, O. Chubykalo-Fesenko, A. Asenjo, Nanomaterials 2022 (1968) 12.
[42] H. Masuda, Fukuda K. science 268 (1995) 1466–1468.
[43] M.J. Donahue, M. Donahue, OOMMF user's guide, version 1.0; US Department of Commerce, National Institute of Standards and Technology (1999).
[44] J.M. MacLaren, T.C. Schulthess, W.H. Butler, R. Sutton, M. McHenry, J. Appl. Phys. 85 (1999) 4833–4835.
[45] J. Zhang, S. Pané, J. Sort, E. Pellicer, Advanced Materials Interfaces 3 (2016) 1600336.
[46] M.P. Proenca, J. Ventura, C.T. Sousa, M. Vazquez, J.P. Araujo, Physical Review B 87 (2013) 134404.
[47] D. Navas, J. Torrejon, F. Béron, C. Redondo, F. Batallan, B.P. Toperverg, A. Devishvili, B. Sierra, F. Castaño, K.R. Pirota, C.A. Ross, New J. Phys. 14 (2012) 113001.
[48] J. Zhang, S. Agramunt-Puig, N. Del-Valle, C. Navau, M.D. Baró, S. Estradé, F. Peiró, S. Pané, B.J. Nelson, A. Sanchez, J. Nogués, E. Pellicer, J. Sort, ACS Applied Materials & Interfaces 8 (2016) 4109–4117.
[49] J. De La Torre Medina, M. Darques, L. Piraux, A. Encinas, J. Appl. Phys. 105 (2009) 023909.
[50] E. Stoner, E. Wohlfarth, IEEE Trans. Magn. 27 (1991) 3475–3518.
[51] V. Vega, T. Böhnert, S. Martens, M. Waleczek, J.M. Montero-Moreno, D. Görlitz, V. Prida, K. Nielsch, Nanotechnology 23 (2012) 465709.
[52] U. Ebels, J.-L. Duvail, P. Wigen, L. Piraux, L. Buda, K. Ounadjela, Physical Review B 64 (2001) 144421.
[53] C. Ramos, E.V. Brigneti, M. Vazquez, Phys. B 354 (2004) 195–197.
[54] others, et al. Journal of Nanoscience and Nanotechnology 2012, 12, 7486–7490
[55] G. Kakazei, A. Kravets, N. Lesnik, M. Pereira de Azevedo, Y.G. Pogorelov, J. Sousa, J. Appl. Phys. 85 (1999) 5654–5656.
[56] G.N. Kakazei, P.E. Wigen, K.Y. Guslienko, R.W. Chantrell, N.A. Lesnik, V. Metlushko, H. Shima, K. Fukamichi, Y. Otani, V. Novosad, J. Appl. Phys. 93 (2003) 8418–8420.
[57] M. Farle, Rep. Prog. Phys. 61 (1998) 755–826.
[58] Y. Velázquez, A.L. Guerrero, J. Martínez, E. Araujo, M.R. Tabasum, B. Nysten, L. Piraux, A. Encinas, Scientific Reports 10 (2020) 21396.
[59] A. Stancu, C. Pike, L. Stoleriu, P. Postolache, D. Cimpoesu, J. Appl. Phys. 93 (2003) 6620–6622.
[60] C.-I. Dobrota, A. Stancu, J. Appl. Phys. 113 (2013) 043928.
[61] C.-I. Dobrota, A. Stancu, Phys. B 457 (2015) 280–286.
[62] E. Jafari-Khamse, M.A. Kashi, A. Ramazani, Curr. Appl. Phys. 16 (2016) 486–496.
[63] J. García, A.M. Manterola, M. Méndez, J.A. Fernández-Roldán, V. Vega, S. González, V.M. Prida, Nanomaterials 11 (2021) 2282.
[64] M. Schöbitz et al., Phys. Rev. Lett. 123 (2019) 217201.
[65] M.P. Proenca, M. Muñoz, I. Villaverde, A. Migliorini, V. Raposo, L. Lopez-Diaz, E. Martinez, J.L. Prieto, Scientific Reports 9 (2019) 17339.
[66] L.G. Vivas, J. Escrig, D.G. Trabada, G.A. Badini-Confalonieri, M. Vázquez, Appl. Phys. Lett. 100 (2012) 252405.
[67] Fernandez-Roldan, J.A.; Perez del Real, R.; Bran, C.; Vazquez, M.; Chubykalo-Fesenko, O. Nanoscale 2018, 10, 5923–5927.
[68] M. Méndez, V. Vega, S. González, R. Caballero-Flores, J. García, V.M. Prida, Nanomaterials 8 (2018) 595.